ORIGINAL PAPER

Effect of temperature on post-yield behavior of PVC foams

Anudeep Reddy Vedire[1] · Michelle S. Hoo Fatt[1] · Akshay Kumar Pakala[1]

Abstract

Experiments were conducted on Divinycell HCP30 foam to develop equations predicting its elastic and post-yield behavior from − 40 to + 60 °C. In these experiments, the foam was subjected to post-yield cyclic tension, compression and shear and monotonic biaxial tension and compression loading in the environmental chamber of an MTS servo-hydraulic machine. Elastic modulus and yield strength of the foam were found to decrease linearly with increasing temperature and could be expressed by a single equation in terms of room temperature properties. Post-yield behavior involved plasticity, viscoelasticity, and damage. An elastic–plastic viscoelastic damage model was used to predict post-yield behavior of the foam at different temperatures. Temperature dependent plastic hardening and viscoelastic damage functions were extracted from the experimental results and used to simulate elastic and post-yield stress–strain behavior in ABAQUS Explicit using a user-defined material subroutine. The ABAQUS user-defined material was validated with experiments on Divinycell HCP30 foam sheets at various temperatures. Good comparisons were found between ABAQUS and experimental results.

Keywords PVC foam · Temperature dependent properties · Post yield

1 Introduction

Polyvinyl chloride (PVC) foam cores are widely used in the core of composite sandwich panels found in the wind energy, aircraft, marine, and transportation industries. The composite sandwich panels in these applications can experience a wide range of environmental temperatures. For example, wind turbine blades are found in parts of Canada where temperatures reach − 40 °C and in the desert of Oman where temperatures regularly exceed + 40 °C. An aircraft is subjected to − 54 °C at an altitude of 10,688 m and may experience up to + 60 °C on the runway. Ships also experience a wide temperature range. Above deck, they are exposed to below freezing temperatures in polar regions, while temperatures approaching + 60 °C frequently occur in the engine room below deck.

Our research addresses elastic and post-yield behavior of PVC foam under temperatures from − 40 to + 60 °C. Post-yielding occurs when foam-core sandwich panels experience impact and impulsive loading. Bird and hail impact on wind turbine blades and blast loading on ship hulls are examples of when these types of loading may occur. The objective of

this research is to characterize and develop predictive equations for describing elastic–plastic behavior of PVC foam in the above-mentioned temperature range. This research is an extension of our previous work, where we examined and modeled the anisotropic, elastic–plastic behavior of Divinycell H100 foam at Arctic cold temperatures, − 40 to 23 °C (Hoo Fatt et al. 2023). In this study, however, our temperature range extends from − 40 to + 60 °C and our focus is on Divinycell HCP30, which is the same as Divinycell H200 foam (DIAB 2023).

There have been few studies on how temperature affects the mechanical behavior of PVC foam cores. At elevated temperatures, the tensile and compressive modulus and strength of PVC foams are much lower than at room temperature (Thomas et al. 2002; Zhang et al. 2012). Zhang et al. (2012) also found that modulus reductions are more significant when temperatures are above 70 °C, and they suggested PVC foam enters a material transition point at around 70 °C. Williams and Lopez-Anido (2014) examined PVC foams in simple shear at − 12, 21 and 60 °C and found that both shear strength and stiffness decreased with increasing temperature. Kim et al. (2023) compared PVC foam properties from 20 °C to as low as − 170 °C. They found both tensile and compressive modulus increased as the temperature decreased over this

✉ Michelle S. Hoo Fatt
  hoofatt@uakron.edu

[1] Department of Mechanical Engineering, The University of Akron, Akron, OH 44325-3903, USA

range. However, the tensile strength decreased while the compressive strength increased as the temperature decreased. Our most recent paper (Hoo Fatt and Vedire 2022) showed that in addition to increased modulus and compressive strength, PVC foams also experienced a substantial reduction in tensile and shear ductility and toughness as the temperature decreased. Ductility and toughness of Divinycell H100 and HCP30 foams were 3–5 times lower at − 60 °C compared to 23 °C. The above-mentioned studies suggest an inverse relationship between elastic modulus and temperature in PVC foams. However, none of these earlier studies dealt with elastic–plastic material properties and material modeling that would be helpful in predicting the crushing behavior of PVC foam at cold or elevated temperatures.

Polymer foams undergo damage, viscoelastic hysteresis, and plasticity when they are being crushed (Hoo Fatt et al. 2021). We developed an anisotropic elastic–plastic viscoelastic damage model for Divinycell H100 foam using a Tsai–Wu yield criterion (Tong et al. 2020) and incorporated this model into ABAQUS Explicit to predict air and underwater blasts of composite sandwich panels (Tong et al. 2021). The Tsai–Wu yield criterion has been shown in Hoo Fat et al. (2021) to be more accurate in predicting initial yielding of PVC foams under multiaxial loading when compared to other anisotropic yield criteria. This anisotropic elastic–plastic viscoelastic damage model will be extended to describe elastic–plastic behavior of Divinycell HCP30 foam at various temperatures.

The following section describes post-yield hysteresis experiments on Divinycell HCP30 at temperatures from − 40 to + 60 °C. Specialized dog-bone and Arcan butterfly specimens and 3D Digital Image Correlation are used to determine post-yield strains in the foam subjected to tension, compression, and shear. In addition to the post-yield hysteresis experiments, Tsai–Wu biaxial yield properties are found by subjecting the foam to monotonic biaxial tension and compression loading at different temperatures. These experimental data are used to describe temperature dependent elastic–plastic viscoelastic damage parameters that can be used to predict post-yield response of the foam at − 40 to + 60 °C. The temperature dependent Divinycell HCP30 foam model will be incorporated into an ABAQUS Explicit user-defined material subroutine. Finally, the foam model is validated by using ABAQUS Explicit to simulate experiments conducted on foam sheet experiments.

2 Materials and specimens

Divinycell HCP30 foam is a closed-wall cellular foam made from a semi-interpenetrating polymer network (semi-IPN) of polyvinyl chloride (PVC) and polyurea (Lindholm et al. 2016). It was manufactured and provided to us as a 25.4 mm-thick panel by DIAB. Cells in the HCP30 foam are more elongated in through-thickness direction giving it transversely isotropic properties.

Arcan butterfly and dog-bone specimens were used to measure strains accurately during post-yielding. The Arcan butterfly specimens were used to obtain shear and compression properties, while the dog-bone specimen was used to obtain tension properties. In conventional shear lap and compression block foam specimens, strains are measured from grip displacements. Strains measured this way are not accurate when there is localized yielding because they are not uniformly distributed throughout the specimen (Wierzbicki and Doyoyo 2002; Taher et al. 2012).

The Arcan butterfly and dog-bone specimens shown in Fig. 1 were machined in various orientations so that both in-plane and out-of-plane properties could be measured. The out-of-plane is denoted by 1–3 axes, whereas the in-plane is denoted by 1–2 axes. Specific dimensions of the Arcan butterfly specimen and the dog-bone specimen can be found in Hoo Fatt et al. (2021). Compression, tension, and shear loadings are indicated on each specimen in Fig. 1, where the solid arrows are for in-plane loading, while the open arrows are for out-of-plane loading. To fully characterize transversely isotropic properties of each foam, tests must be conducted in the six modes shown in Fig. 1. Because the foam is transversely isotropic, properties in the 1–3 and 2–3 planes are the same.

For biaxial tests, modified Maltese cross specimens were cut from the panels in the out-of-plane and in-plane orientations shown in Fig. 2. Dimensions of Maltese cross specimen allow for plane stress conditions and are given in Appendix A. Tension and compression loadings on the Maltese cross specimens are shown in Fig. 2. where again the solid arrows are for in-plane loading and open arrows are for out-of-plane loading. The Maltese cross specimens were placed in a specially designed biaxial test fixture, which will be explained later.

Specimens were spray painted white and then speckled with black spray paint. After painting, specimens were placed into the oven or freezer to the appropriate test temperatures for a minimum of two days or 48 h. Specimens experiencing tension or shear were glued into holders using J-B Weld Pro Blister Epoxy (a cold-weld, two-part epoxy system) before the 48 h-minimum heating or freezing cycle. These holders are connected to specialized grips during the test, as will be explained in the next section.
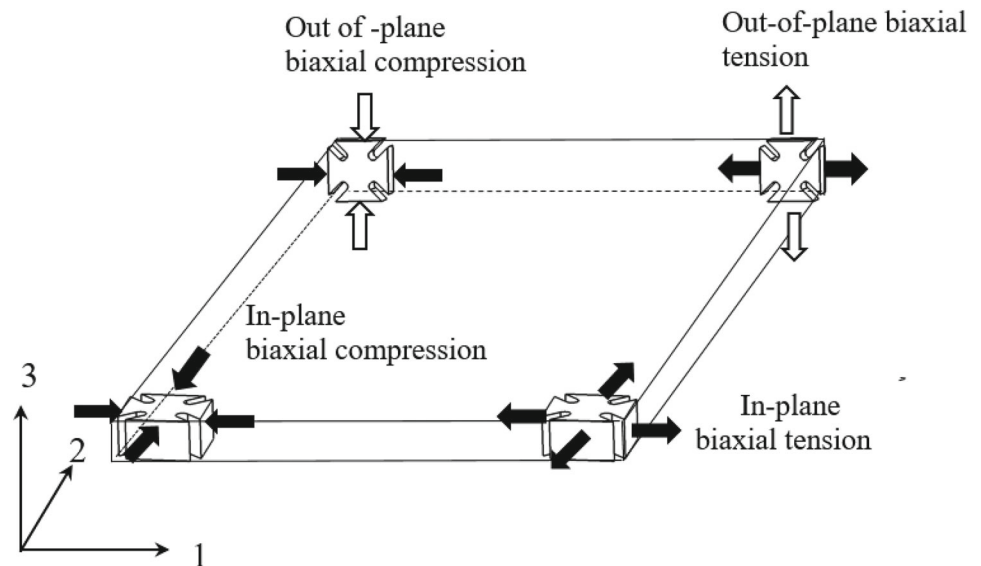
3 Experiments

An MTS 831 servo-hydraulic machine, equipped with an environmental chamber, was used to perform uniaxial compression and tension and shear tests and the biaxial tension and compression tests at various temperatures.

Fig. 1 Compression, tension and shear specimen orientations and loadings
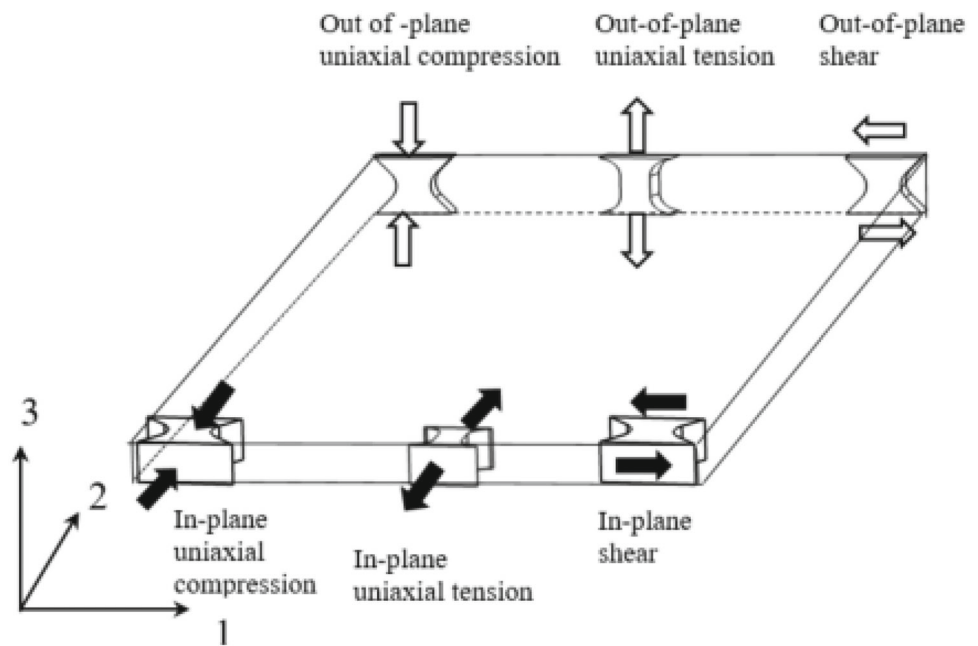
Fig. 2 Maltese cross specimen orientations and loading


3.1 Uniaxial and shear hysteresis

Specimens in compression, tension and shear inside the chamber are shown in Fig. 3a–c. The compression specimen was compressed between steel pucks. The holders of the tension and shear specimens were fitted into grips with universal ball joints, which were aligned along the center of specimen. Perfect alignment of the load transmitted through the ball joint was critical in achieving simple shear without any twist or bend in the shear specimen. Digital Image Correlation was used to find full-field strains of the specimens, while the stress in the specimen was calculated from the loads recorded by the load cell of the MTS machine. Specimens were cyclically loaded under displacement-control to produce 4–5 hysteresis loops beyond the initial yield point. Each test was performed at a constant displacement rate of 1.27 mm/s and at + 60, + 40, + 23, 0, − 20 and − 40 °C.

3.2 Biaxial tension and compression yield points

These experiments were conducted to find Tsai–Wu biaxial yield coefficients, which will be defined later. The specialized 4-bar link apparatus shown in Fig. 4a was developed for the biaxial experiments. The 4-bar link apparatus consists of four pinned-ended bars, each attached to a central joint

Fig. 3 Specimens in the chamber: **a** compression, **b** shear and **c** tension
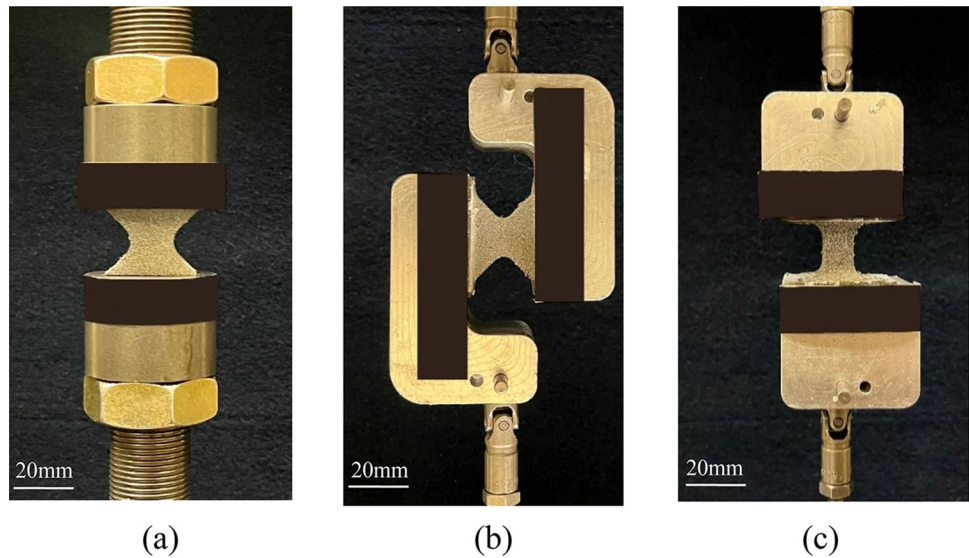
Fig. 4 Biaxial experimental setup: **a** 4-bar link apparatus and **b** planar Maltese cross specimen
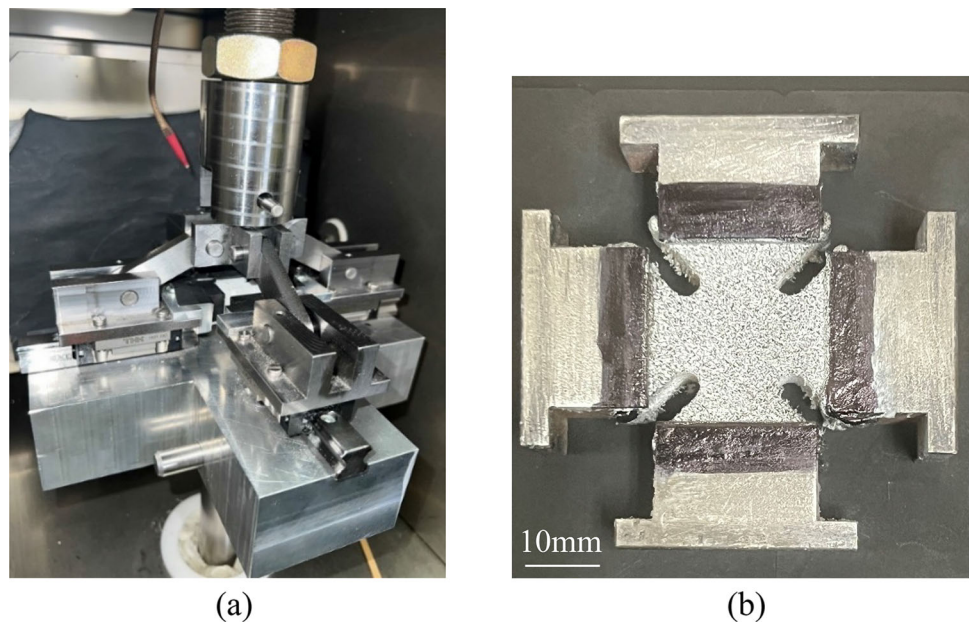
connected to the actuator arm of the MTS machine and a linear bearing. Four sides of the specimen are attached to grips that are mounted on linear bearings. Figure 4b shows the tension Maltese cross specimen, which is glued into holders and would fit into these grips. Motion of the grips are controlled by slider bars. When the actuator moves up, the slider bars move inward thereby causing biaxial compression. Conversely, when the actuator moves down, the slider bars move outward putting the specimen in biaxial tension. Similar 4-bar designs can be found in Barroso et al. (2018), Medellín and Diosdado De la Peña (2017). The Maltese cross specimens were monotonically loaded under displacement-control at a constant displacement rate of 1.27 mm/s. This was done at + 60, + 40, + 23, 0, − 20 and − 40 °C.

4 Compression, shear and tension post-yield hysteresis

The out-of-plane DIC strain distributions in the compression, shear and tension specimens are shown in Fig. 5. In all the modes, yielding is localized to a central neck region. Compression buckling of foam cells was localized to the neck of the Arcan butterfly specimen. This neck extends over a region, about 10 mm in length, and compression strains were averaged in this region. Shear strain localization occurred in the neck of the Arcan butterfly specimen, while uniform strain occurred along the center gage of the dog-bone specimen. Both shear and tensile strains were calculated by averaging values along the centerline of the gage.

Fig. 5 Full-field DIC strain fields in compression, shear, and tension

compression   shear   tension
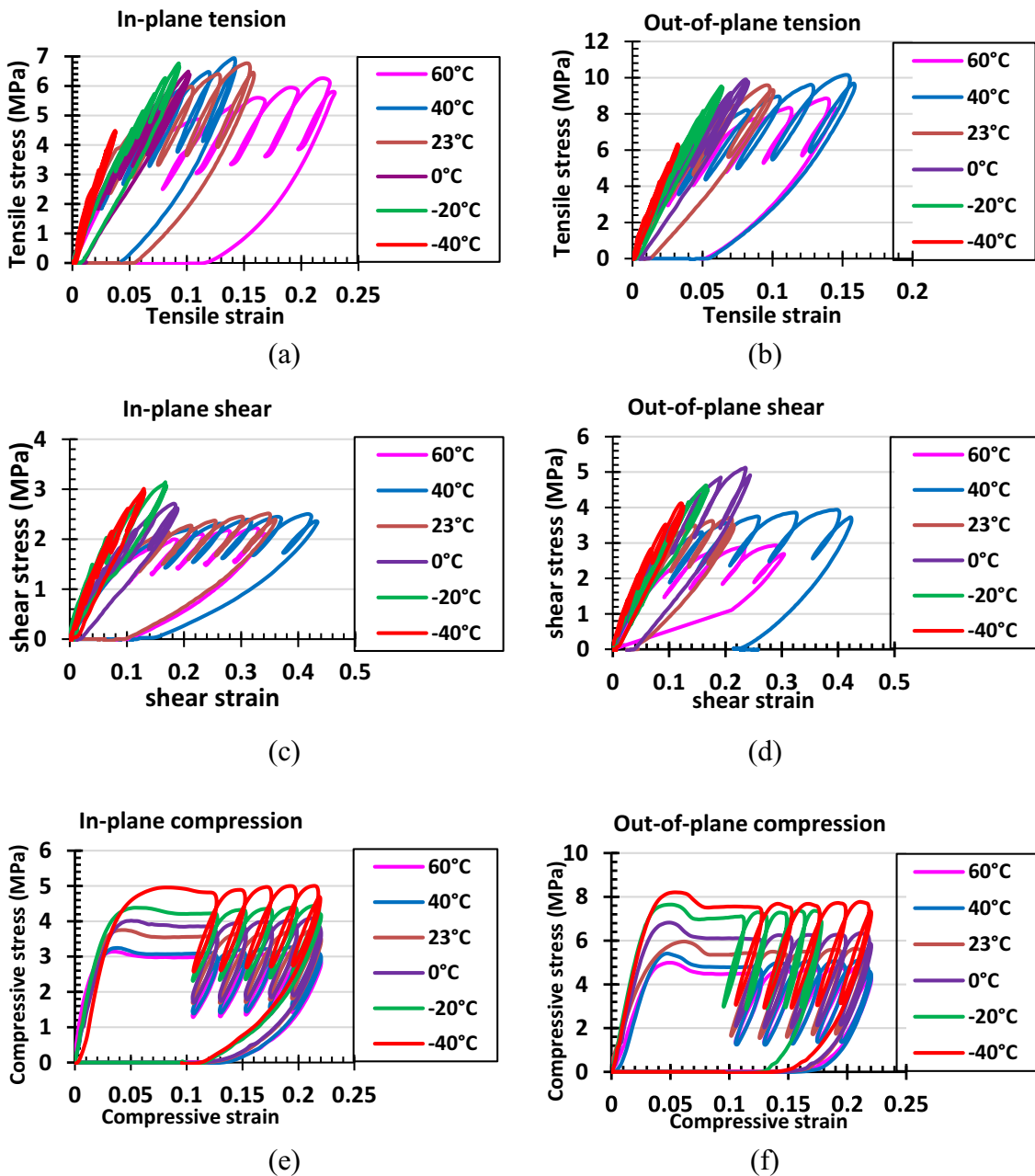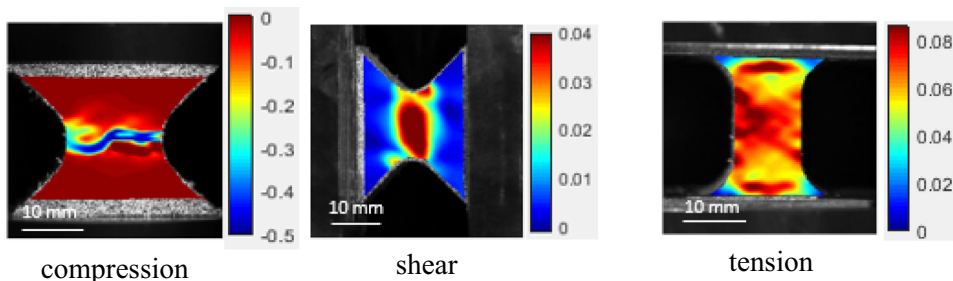
Fig. 6 Post-yield hysteresis at various temperatures: **a** in-plane tension, **b** out-of-plane tension, **c** in-plane shear, **d** out-of-plane shear, **e** in-plane compression and **f** out-of-plane compression

Post-yield hysteresis of Divinycell HCP30 foam in all six modes of loading are given in Fig. 6a–f. It can be observed that the elastic modulus and yield strength increase as the temperature decreases from $+60$ to $-40\ °C$ in all cases. The compression modulus is almost twice the tensile modulus. The strain range in tension and shear was reduced for colder temperatures because HCP30 foam becomes more brittle as the temperature falls from $+60$ to $-40\ °C$. In Hoo Fatt et al. (2023), a ductile-to-brittle transition point was found at around $-50\ °C$. Energy dissipation in cyclic loading is represented in each hysteresis loop with viscoelastic damping and internal damage of cells. It can also be observed that in every stress–strain curve, as the cyclic loading progresses, the thickness of the loop increases, and the modulus decreases indicating the damage.

5 Biaxial yield strengths

The biaxial yield strengths are determined from the stress yield points in the Maltese cross specimen. As described in Appendix C, yield strength is loss of linearity in force–deformation response. The yield point is determined on the load–displacement curve by extrapolating a straight line in the initial linear region. The point where the curve is deviated from the straight line is defined as the yield point. Figure 7a, b show the yield surfaces of Divinycell HCP30 foams at temperatures ranging from -40 to $60\ °C$ for the in-plane and out-of-plane Maltese cross specimens, respectively. The yield surfaces grow outward as the temperature decreases. This trend is to be expected since yield strengths increase with decreasing temperatures.

6 Material constitutive equations

An elastic plastic viscoelastic damage model, which was developed for room temperature response of Divinycell H100 foam (Tong et al. 2021), is extended to account for temperature dependent behavior of Divinycell HCP30 foam. The foam material model is described in Fig. 8a, b. Before yielding and irreversible damage of cells, the foam experiences linear elastic behavior where $\mathbf{C}_0$ is the elastic stiffness matrix and $\boldsymbol{\varepsilon}$ represents strain. After initial yielding and irreversible damage, the foam undergoes plasticity, damage, and viscoelastic hysteresis. The total strain $\boldsymbol{\varepsilon}$ decomposes into elastic and plastic components, $\boldsymbol{\varepsilon}_e$ and $\boldsymbol{\varepsilon}_p$, respectively. The Tsai Wu yield criterion and associated flow rule $\boldsymbol{\sigma}_y$, determines whether plastic flow occurs. Viscoelastic hysteresis is described with a simple Maxwell model, an equilibrium spring of stiffness $\overline{\mathbf{C}}_0$ in parallel with an intermediate spring of stiffness $\overline{\mathbf{C}}_{ev}$ and viscous damper $\overline{\mathbf{V}}$. The overhead bar denotes that stiffness and viscosity are damage dependent.

Material properties $\mathbf{C}_0$, $\boldsymbol{\sigma}_y$, $\overline{\mathbf{C}}_0$, $\overline{\mathbf{C}}_{ev}$, and $\overline{\mathbf{V}}$ vary with temperature.

The Cauchy stress $\boldsymbol{\sigma}$ and true strain $\boldsymbol{\varepsilon}$ are expressed in Voigt notation:

$$\boldsymbol{\sigma} = \left(\begin{array}{cccccc} \sigma_x & \sigma_y & \sigma_z & \tau_{xy} & \tau_{zx} & \tau_{yz} \end{array} \right)^T \tag{1}$$

and

$$\boldsymbol{\varepsilon} = \left(\begin{array}{cccccc} \varepsilon_x & \varepsilon_y & \varepsilon_z & \gamma_{xy} & \gamma_{zx} & \gamma_{yz} \end{array} \right)^T \tag{2}$$

Here the x- and y-coordinates are in the in-plane direction of the foam, while the z-coordinate is in the out-of-plane direction of the foam. Material behavior is described in the following three parts.

6.1 Orthotropic linear elastic response

The stress is given by

$$\boldsymbol{\sigma} = \mathbf{C}_0 \boldsymbol{\varepsilon} \tag{3}$$

where $\mathbf{C}_0$ is the stiffness matrix given by

$$\mathbf{C}_0 = \begin{bmatrix} C_{11} & C_{12} & C_{13} & 0 & 0 & 0 \\ C_{12} & C_{22} & C_{23} & 0 & 0 & 0 \\ C_{13} & C_{23} & C_{33} & 0 & 0 & 0 \\ 0 & 0 & 0 & C_{44} & 0 & 0 \\ 0 & 0 & 0 & 0 & C_{55} & 0 \\ 0 & 0 & 0 & 0 & 0 & C_{66} \end{bmatrix}$$

and

$$C_{11} = \frac{(E_{22} - v_{23}^2 E_{33})E_{11}^2}{\Omega}$$

$$C_{12} = \frac{(v_{12}E_{22} + v_{13}v_{23}E_{33})E_{11}E_{22}}{\Omega}$$

$$C_{13} = \frac{(v_{12}v_{23} + v_{13})E_{11}E_{22}E_{33}}{\Omega}$$

$$C_{22} = \frac{(E_{11} - v_{13}^2 E_{33})E_{22}^2}{\Omega}$$

$$C_{23} = \frac{(v_{23}E_{11} + v_{12}v_{13}E_{22})E_{22}E_{33}}{\Omega}$$

$$C_{33} = \frac{(E_{11} - v_{12}^2 E_{22})E_{22}E_{33}}{\Omega}$$

$$C_{44} = G_{23} \quad C_{55} = G_{13} \quad C_{66} = G_{12}$$

and $\Omega = E_{11}E_{22} - v_{12}^2 E_{22}^2 - v_{13}^2 E_{22}E_{33} - v_{23}^2 E_{11}E_{33} - 2v_{12}v_{13}v_{23}E_{22}E_{33}$.
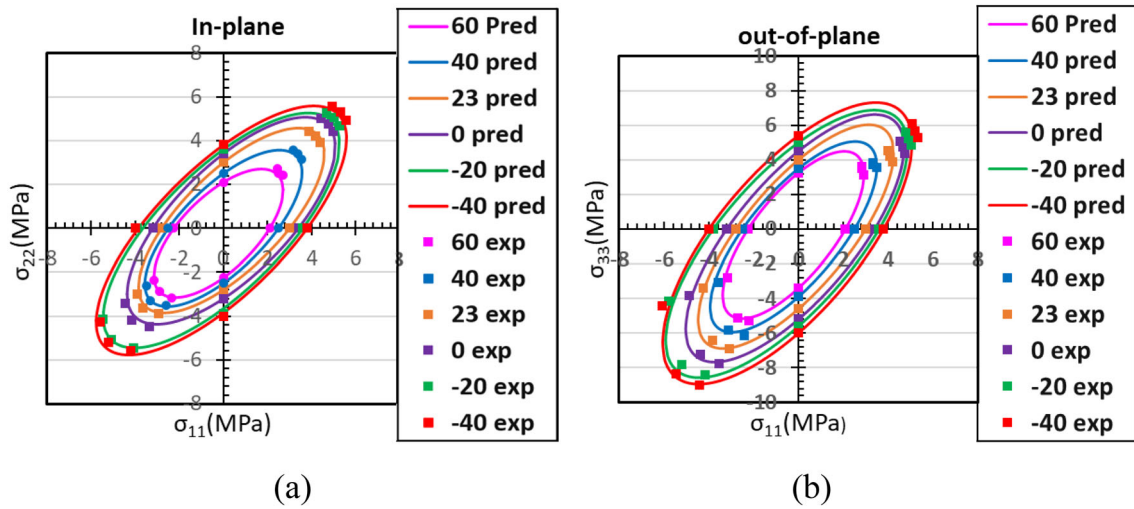
Fig. 7 Biaxial yield surfaces: **a** in-plane and **b** out-of-plane

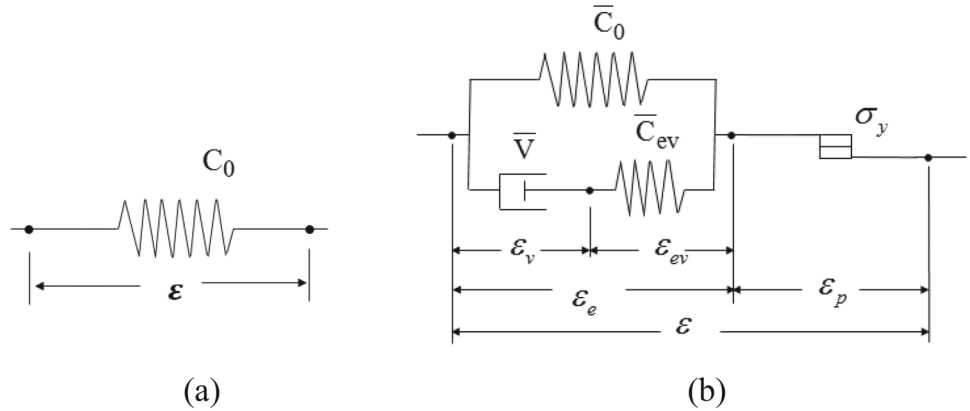**Fig. 8** Foam model: **a** before initial yielding/damage and **b** after initial yielding/damage

Table 1 Room temperature elastic properties of Divinycell HCP30 foam

$E_{11t} = E_{22t}$(MPa)	E_{33t} (MPa)	$E_{11c} = E_{22c}$(MPa)	E_{33c} (MPa)	G_{12}(MPa)	$G_{13} = G_{23}$(MPa)	ν_{12}	ν_{31}
85	172	165	273	22	36	0.37	0.4

Poisson's ratios do not vary with temperature and are given in Table 1. However, the elastic modulus varies with temperature as shown in Fig. 9. The following analytical expression describes the variation of elastic modulus with temperature in terms of the room temperature values given in Table 1:

$$E / E_{23} = -0.0065T + 1.14 \tag{4}$$

where E is the modulus in a particular mode, E_{23} is the room temperature modulus in the same mode, and T is temperature in ºC. Predicted results using Eq. (4) are also shown in Fig. 9.

6.2 Initial yield/damage

In Hoo Fatt et al. (2021), the Tsai–Wu yield criterion was compared to other anisotropic yield criteria and shown to be more accurate in predicting initial yielding of PVC foam under triaxial stress. The PVC foam was subjected to pressure and shear among other triaxial loading cases in Hoo Fatt et al. (2021). The Tsai–Wu yield function fits experimental results for multiaxial foam yielding better than others because of its ability to distinguish between tension and compression yield strengths and it offers many interaction coefficients that could be fitted to multiaxial test results. For an orthotropic material, the Tsai–Wu criterion is conveniently expressed as

$$\frac{1}{2}\sigma\mathbf{P}\sigma^T + \mathbf{q}^T\sigma = 1 \tag{5}$$
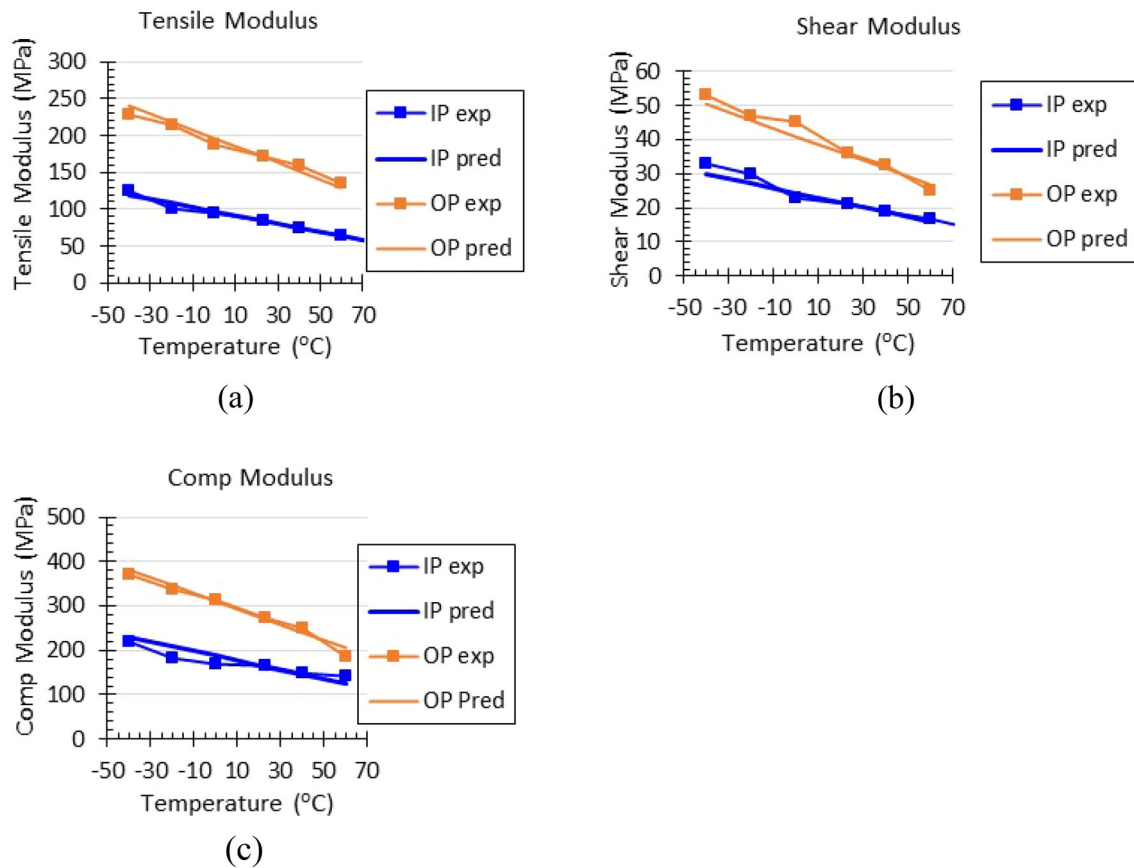
Fig. 9 Temperature variation of Divinycell HCP30 foam elastic modulus: **a** tension, **b** shear, and **c** compression

where

$$\mathbf{P} = 2\begin{bmatrix} X_{11} & X_{12} & X_{13} & 0 & 0 & 0 \\ X_{12} & X_{22} & X_{23} & 0 & 0 & 0 \\ X_{13} & X_{23} & X_{33} & 0 & 0 & 0 \\ 0 & 0 & 0 & X_{44} & 0 & 0 \\ 0 & 0 & 0 & 0 & X_{55} & 0 \\ 0 & 0 & 0 & 0 & 0 & X_{66} \end{bmatrix}$$

and

$$\mathbf{q} = \begin{bmatrix} X_1 & X_2 & X_3 & 0 & 0 & 0 \end{bmatrix}^T$$

and $X_1 = \frac{1}{f_1^t} - \frac{1}{f_1^c}$, $X_2 = \frac{1}{f_2^t} - \frac{1}{f_2^c}$, $X_3 = \frac{1}{f_3^t} - \frac{1}{f_3^c}$, $X_{11} = \frac{1}{f_1^t f_1^c}$, $X_{22} = \frac{1}{f_2^t f_2^c}$, $X_{33} = \frac{1}{f_3^t f_3^c}$, $X_{44} = \left(\frac{1}{f_{23}}\right)^2$, $X_{55} = \left(\frac{1}{f_{13}}\right)^2$, $X_{66} = \left(\frac{1}{f_{12}}\right)^2$, X_{12}, X_{13} and X_{23} are interaction coefficient terms, f_i^t and f_i^c are tensile and compressive yield strengths in the $i = 1, 3$ direction and f_{ij} is the shear yield strength associated with the ij-plane ($i, j = 1, 3$). The interaction coefficients, X_{12}, X_{13} and X_{23} are obtained from the biaxial tests. For a transversely isotropic material, $X_2 = X_1$, $X_{22} = X_{11}$, $X_{55} = X_{44}$ and the interaction

coefficients reduce specifically to X_{12} and $X_{13} = X_{23}$. Tsai (1984) explains that for transversely isotropic material that is isotropic in the 1–2 plane $X_{12} = X_{11} - \frac{1}{2}X_{66}$. Li et al. (2017) gives a thorough discussion on how Tsai Wu interaction term affects yield surfaces in the context of unidirectional composite laminates.

The following equation describes temperature variation of yield strengths in terms of room temperature values in Table 2:

$$\sigma_y/\sigma_{y23} = -0.0065T + 1.14 \tag{6}$$

where σ_y is the yield strength in a particular mode, σ_{23} is the room temperature yield strength in the same mode, and T is temperature in °C. Note that Eq. (6) is identical to Eq. (5) because yielding is determined by loss of linearity. Both experimental and analytical predictions from Eq. (6) are shown in Fig. 10.

The biaxial yield strengths shown in Fig. 7a, b are fitted with the Tsai-Wu yield function and uniaxial and shear yield strengths to find X_{12} and $X_{13} = X_{23}$ at various temperatures. These curve fits are shown in Fig. 7a, b, and temperature variations of X_{12} and $X_{13} = X_{23}$ are shown in Fig. 11. It can
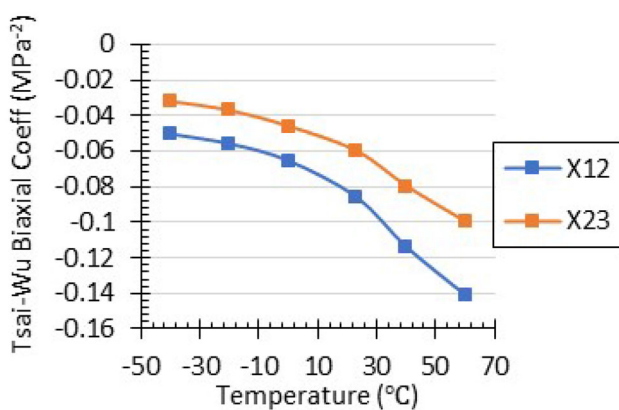
Table 2 Room temperature yield strengths of Divinycell HCP30 foam

$X_{ty} = Y_{ty}$(MPa)	$X_{cy} = Y_{cy}$(MPa)	Z_{ty}(MPa)	Z_{cy} (MPa)	S_{y12} (MPa)	$S_{y13} = S_{y23}$ (MPa)
3	2.8	4	4.6	1.2	2.2

(a)

(b)

(c)
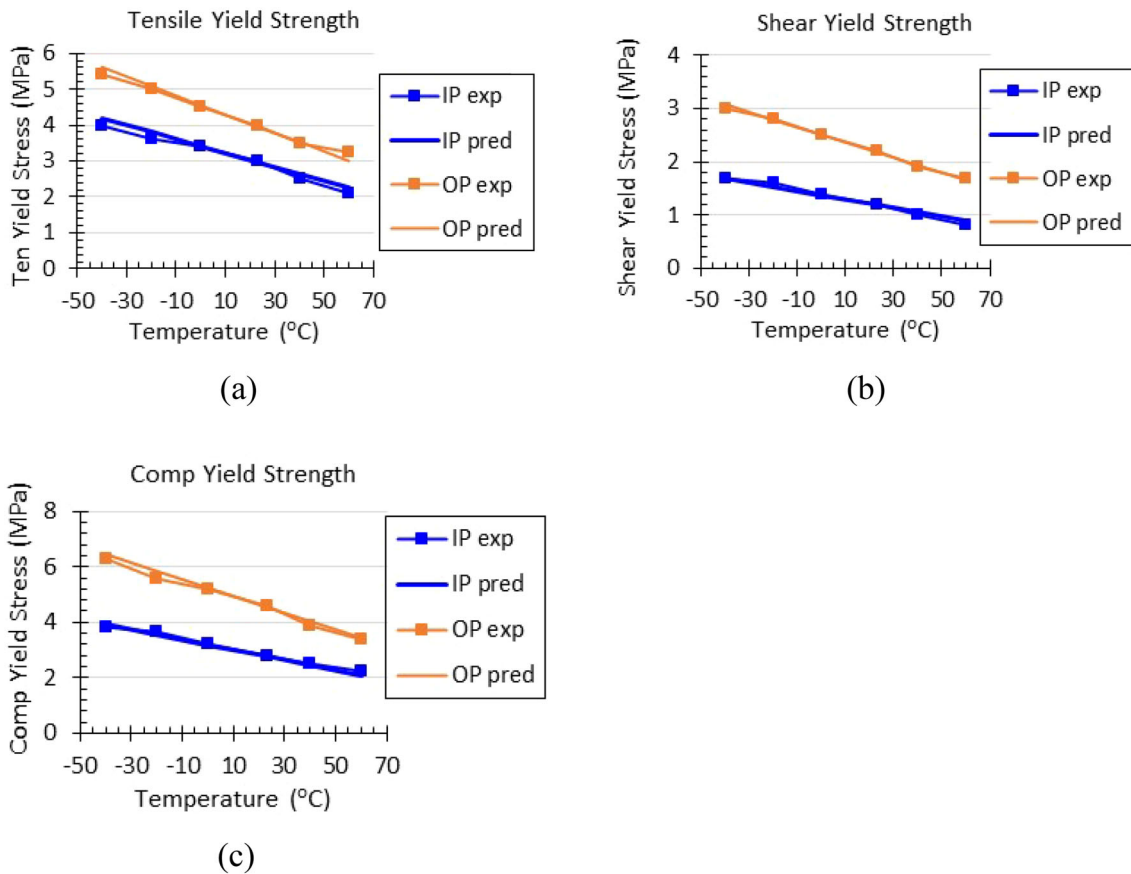
Fig. 10 Temperature variation of Divinycell HCP30 foam yield strengths: **a** tension, **b** shear, and **c** compression

Fig. 11 Temperature variation of Tsai–Wu biaxial coefficients: X_{12} and $X_{13} = X_{23}$.

also be confirmed that $X_{12} = X_{11} - \frac{1}{2}X_{66}$ during the curve fitting of the experimental results in Fig. 7a.

6.3 Anisotropic hardening and viscoelastic damage response

Anisotropic hardening takes place during plastic flow, while viscoelastic hysteresis occurs during unloading and reloading. Once the foam has yielded, cells are damaged, and both plastic and viscoelastic properties must take this damage into account.

6.3.1 Anisotropic hardening

Following Tong et al. (2021), a reduced stress state is used to account for anisotropic hardening in the Tsai–Wu yield criterion during continued plastic flow. The actual stress $\boldsymbol{\sigma}$ is related to the reduced stress $\hat{\boldsymbol{\sigma}}$ by a hardening matrix:

$$\mathbf{s} = \mathbf{H}\hat{\boldsymbol{\sigma}} \tag{7}$$
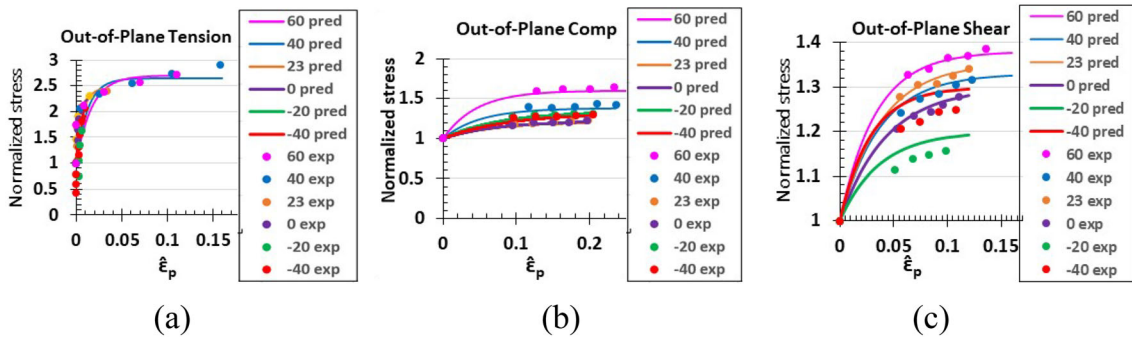
Fig. 12 Out-of-Plane hardening **a** tension, **b** compression and **c** shear
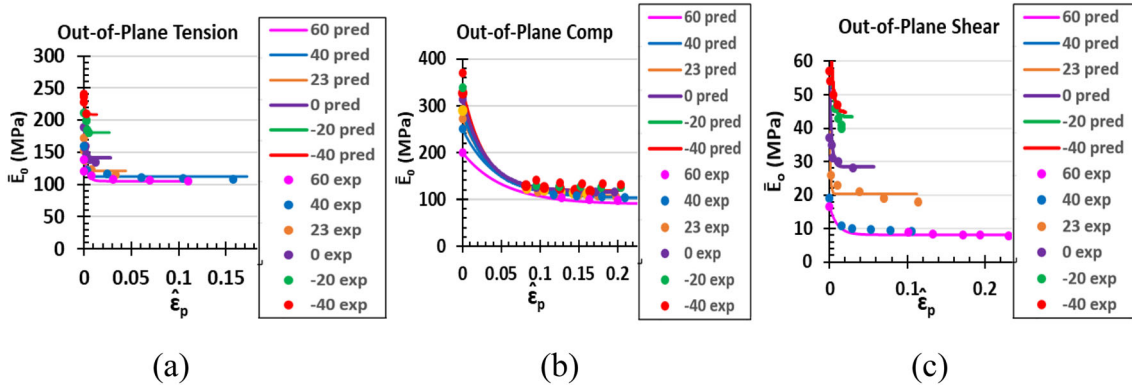

Fig. 13 Out-of-plane $\overline{E}_0$: **a** tension, **b** compression and **c** shear
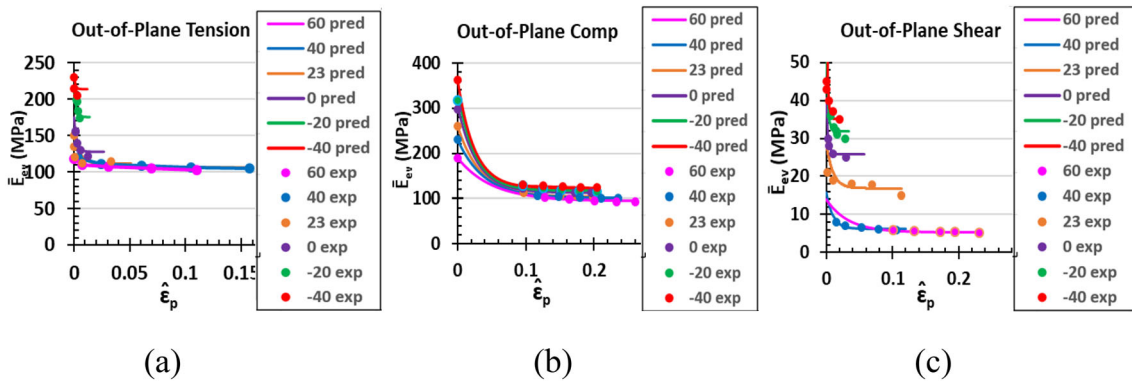

Fig. 14 Out-of-plane $\overline{E}_{ev}$: **a** tension, **b** compression and **c** shear

where

and H_{ij} is the normalized flow stress obtained from uniaxial and shear tests as

$$\mathbf{H} = \begin{bmatrix} H_{11} & 0 & 0 & 0 & 0 & 0 \\ 0 & H_{22} & 0 & 0 & 0 & 0 \\ 0 & 0 & H_{33} & 0 & 0 & 0 \\ 0 & 0 & 0 & H_{23} & 0 & 0 \\ 0 & 0 & 0 & 0 & H_{13} & 0 \\ 0 & 0 & 0 & 0 & 0 & H_{12} \end{bmatrix}$$

$$H_{ij} = \begin{cases} \dfrac{|\sigma_{ijc}|}{f_i^c} & i = j, \, compression \\[2ex] \dfrac{\sigma_{ijt}}{f_i^t} & i = j, \, tension \\[2ex] \dfrac{\tau_{ijt}}{f_{ij}} & i \neq j, \, shear \end{cases}$$
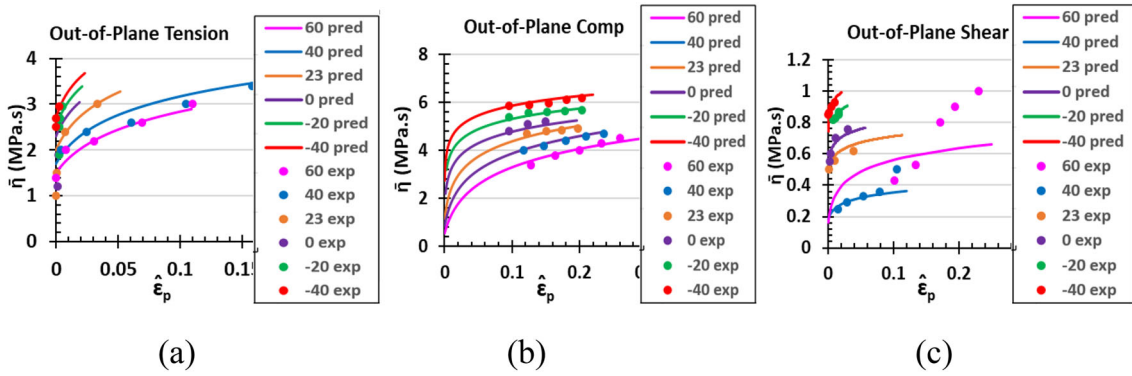
Fig. 15 Out-of-plane $\overline{\eta}$: **a** tension, **b** compression and **c** shear

The plastic potential function is then defined in terms of a reduced stress $\hat{\sigma}$ such that

$$\Phi = \frac{1}{2}\hat{\sigma}^T \mathbf{P}\hat{\sigma} + \mathbf{q}^T\hat{\sigma} - 1 \qquad (8)$$

Substituting $\hat{\sigma} = \mathbf{H}^{-1}\sigma$ into Eq. (8) gives

$$\Phi = \frac{1}{2}\sigma^T \hat{\mathbf{P}}\sigma + \hat{\mathbf{q}}^T\sigma - 1 \qquad (9)$$

where $\hat{\mathbf{P}} = \mathbf{H}^{-T}\mathbf{P}\mathbf{H}^{-1}$ and $\hat{\mathbf{q}} = \mathbf{H}^{-T}\mathbf{q}$.

Using the associated flow rule, we derive the plastic strain component $d\varepsilon_p$ from Eq. (9) as

$$d\boldsymbol{\varepsilon}_{\mathbf{p}} = \dot{\lambda}\frac{d\Phi}{d\sigma} = \dot{\lambda}\left(\hat{\mathbf{P}}\sigma + \hat{\mathbf{q}}\right) \qquad (10)$$

where the plastic multiplier $\dot{\lambda}$ has unit of stress. From conjugate work theory, we get

$$\sigma_e d\overline{\varepsilon}_p = \sigma^T d\boldsymbol{\varepsilon}_{\mathbf{p}} \qquad (11)$$

where $\overline{\varepsilon}_p$ is equivalent plastic strain and σ_e is equivalent stress. Conjugate work theory may also be expressed in terms of the reduced equivalent stress $\hat{\sigma}_e$ and the reduced equivalent plastic strain $\hat{\varepsilon}_p$

$$\sigma_e d\overline{\varepsilon}_p = \hat{\sigma}_e d\hat{\varepsilon}_p \qquad (12)$$

Hence, Eq. (11) becomes

$$\hat{\sigma}_e d\hat{\varepsilon}_p = \sigma^T d\boldsymbol{\varepsilon}_{\mathbf{p}} \qquad (13)$$

The reduced equivalent stress $\hat{\sigma}_e$ is defined by

$$\hat{\sigma}_e = f_{33}^c \sqrt{\frac{1}{2}\sigma^T \hat{\mathbf{P}}\sigma + \hat{\mathbf{q}}^T\sigma} \qquad (14)$$

where f_{33}^c is the compressive yield strength in the through-thickness direction. During plastic flow $\Phi = 0$ and

$\sqrt{\frac{1}{2}\sigma^T \hat{\mathbf{P}}\sigma + \hat{\mathbf{q}}^T\sigma} = 1$, so that the equivalent reduced stress becomes

$$\hat{\sigma}_e = f_{33}^c \qquad (15)$$

Substituting Eq. (15) into Eq. (13) gives an expression for the reduced equivalent plastic strain increment $d\hat{\varepsilon}_p$ as

$$d\hat{\varepsilon}_p = \frac{\sigma^T}{f_{33}^c}d\boldsymbol{\varepsilon}_{\mathbf{p}} \qquad (16)$$

Using Eq. (10) to eliminate $d\varepsilon_p$ in Eq. (16) gives

$$d\hat{\varepsilon}_p = \frac{\sigma^T}{f_{33}^c}\dot{\lambda}\left(\hat{\mathbf{P}}\sigma + \hat{\mathbf{q}}\right) = \frac{\dot{\lambda}}{f_{33}^c}\left(\sigma^T \hat{\mathbf{P}}\sigma + \hat{\mathbf{q}}^T\sigma\right) \qquad (17)$$

Once again during plastic flow $\Phi = 0$ and $\sigma^T \hat{\mathbf{P}}\sigma + 2\hat{\mathbf{q}}^T\sigma = 2$, and Eq. (17) can be simplified to

$$d\hat{\varepsilon}_p = \frac{\dot{\lambda}}{f_{33}^c}\left(2 - \hat{\mathbf{q}}^T\sigma\right) \qquad (18)$$

The reduced equivalent plastic strain $\hat{\varepsilon}_p$ is one of the state variables that will be used in this constitutive model to describe the anisotropic hardening functions H_{ij} and the damage material properties, $\overline{E}_{ii}$, $\overline{G}_{ij}$, $\overline{E}_{evii}$, $\overline{G}_{evij}$ and $\overline{\eta}_{ij}$, which will be defined in the following section.

6.3.2 Viscoelastic damage

When $\Phi < 0$, the standard viscoelastic model in Fig. 8b is used to provide a viscoelastic damage response. The total stress is given as the sum of equilibrium stress and overstress:

$$\sigma = \sigma_{eq} + \sigma_{ov} \qquad (19)$$

The equilibrium stress σ_{eq} is

$$\sigma_{eq} = \overline{\mathbf{C}}_0\left(\varepsilon - \varepsilon_p\right) \qquad (20)$$

where $\overline{\mathbf{C}}_0$ is the damage stiffness matrix of the equilibrium spring, which is similar to $\mathbf{C}_0$ but with damage elastic moduli, $\overline{E}_{ij}$. The overstress $\boldsymbol{\sigma}_{ov}$ is

$$\boldsymbol{\sigma}_{ov} = \overline{\mathbf{C}}_{ev}\boldsymbol{\varepsilon}_{ev} \tag{21}$$

where $\overline{\mathbf{C}}_{ev}$ is the stiffness matrix of the intermediate spring given by

$$\overline{\mathbf{C}}_{ev} = \begin{bmatrix} \overline{C}_{ev11} & \overline{C}_{ev12} & \overline{C}_{ev13} & 0 & 0 & 0 \\ \overline{C}_{ev12} & \overline{C}_{ev22} & \overline{C}_{ev23} & 0 & 0 & 0 \\ \overline{C}_{ev13} & \overline{C}_{ev23} & \overline{C}_{ev33} & 0 & 0 & 0 \\ 0 & 0 & 0 & \overline{C}_{ev44} & 0 & 0 \\ 0 & 0 & 0 & 0 & \overline{C}_{ev55} & 0 \\ 0 & 0 & 0 & 0 & 0 & \overline{C}_{ev66} \end{bmatrix}$$

and

$$\overline{C}_{ev11} = \frac{(\overline{E}_{ev22} - v_{23}^2 \overline{E}_{ev33})\overline{E}_{ev11}^2}{\Phi}$$

$$\overline{C}_{ev12} = \frac{(v_{12}\overline{E}_{ev22} + v_{13}v_{23}\overline{E}_{ev33})\overline{E}_{ev11}\overline{E}_{ev22}}{\Phi}$$

$$\overline{C}_{ev13} = \frac{(v_{12}v_{23} + v_{13})\overline{E}_{ev11}\overline{E}_{ev22}\overline{E}_{ev33}}{\Phi}$$

$$\overline{C}_{ev22} = \frac{(\overline{E}_{ev11} - v_{13}^2 \overline{E}_{ev33})\overline{E}_{ev22}^2}{\Phi}$$

$$\overline{C}_{ev23} = \frac{(v_{23}\overline{E}_{ev11} + v_{12}v_{13}\overline{E}_{ev22})\overline{E}_{ev22}\overline{E}_{ev33}}{\Phi}$$

$$\overline{C}_{ev33} = \frac{(\overline{E}_{ev11} - v_{12}^2 \overline{E}_{ev22})\overline{E}_{ev22}\overline{E}_{ev33}}{\Phi}$$

$$\overline{C}_{ev33} = \frac{(\overline{E}_{ev11} - v_{12}^2 \overline{E}_{ev22})\overline{E}_{ev22}\overline{E}_{ev33}}{\Phi}$$

$$\overline{C}_{ev44} = \overline{G}_{ev23} \quad \overline{C}_{ev55} = \overline{G}_{ev13} \quad \overline{C}_{ev66} = \overline{G}_{ev12}$$

and $\Phi = \overline{E}_{ev11}\overline{E}_{ev22} - v_{12}^2\overline{E}_{ev22}^2 - v_{13}^2\overline{E}_{ev22}\overline{E}_{ev33} - v_{23}^2\overline{E}_{ev11}\overline{E}_{ev33} - 2v_{12}v_{13}v_{23}\overline{E}_{ev22}\overline{E}_{ev33}$.

Compatibility of strain requires that

$$\boldsymbol{\varepsilon} = \boldsymbol{\varepsilon}_p + \boldsymbol{\varepsilon}_{ev} + \boldsymbol{\varepsilon}_v \tag{22}$$

Using Eq. (22) to eliminate $\boldsymbol{\varepsilon}_{ev}$ in Eq. (21) gives

$$\boldsymbol{\sigma}_{ov} = \overline{\mathbf{C}}_{ev}(\boldsymbol{\varepsilon} - \boldsymbol{\varepsilon}_p - \boldsymbol{\varepsilon}_v) \tag{23}$$

The overstress is also governed by a linear viscosity law:

$$\boldsymbol{\sigma}_{ov} = \overline{\mathbf{V}}\dot{\boldsymbol{\varepsilon}}_v \tag{24}$$

where $\overline{\mathbf{V}}$ is the viscosity matrix given by

$$\overline{\mathbf{V}} = \begin{bmatrix} \overline{V}_{11} & \overline{V}_{12} & \overline{V}_{13} & 0 & 0 & 0 \\ \overline{V}_{12} & \overline{V}_{22} & \overline{V}_{23} & 0 & 0 & 0 \\ \overline{V}_{13} & \overline{V}_{23} & \overline{V}_{33} & 0 & 0 & 0 \\ 0 & 0 & 0 & \overline{V}_{44} & 0 & 0 \\ 0 & 0 & 0 & 0 & \overline{V}_{55} & 0 \\ 0 & 0 & 0 & 0 & 0 & \overline{V}_{66} \end{bmatrix}$$

and

$$\overline{V}_{11} = \frac{(\overline{\eta}_{22} - v_{23}^2\overline{\eta}_{33})\overline{\eta}_{11}^2}{\Psi}$$

$$\overline{V}_{12} = \frac{(v_{12}\overline{\eta}_{22} + v_{13}v_{23}\overline{\eta}_{33})\overline{\eta}_{11}\overline{\eta}_{22}}{\Psi}$$

$$\overline{V}_{13} = \frac{(v_{12}v_{23} + v_{13})\overline{\eta}_{11}\overline{\eta}_{22}\overline{\eta}_{33}}{\Psi}$$

$$\overline{V}_{22} = \frac{(\overline{\eta}_{11} - v_{13}^2\overline{\eta}_{33})\overline{\eta}_{22}^2}{\Psi}$$

$$\overline{V}_{23} = \frac{(v_{23}\overline{\eta}_{11} + v_{12}v_{13}\overline{\eta}_{22})\overline{\eta}_{22}\overline{\eta}_{33}}{\Psi}$$

$$\overline{V}_{33} = \frac{(\overline{\eta}_{11} - v_{12}^2\overline{\eta}_{22})\overline{\eta}_{22}\overline{\eta}_{33}}{\Psi}$$

$$\overline{V}_{44} = \overline{\eta}_{23} \quad \overline{V}_{55} = \overline{\eta}_{13} \quad \overline{V}_{66} = \overline{\eta}_{12}$$

and $\Psi = \overline{\eta}_{11}\overline{\eta}_{22} - v_{12}^2\overline{\eta}_{22}^2 - v_{13}^2\overline{\eta}_{22}\overline{\eta}_{33} - v_{23}^2\overline{\eta}_{11}\overline{\eta}_{33} - 2v_{12}v_{13}v_{23}\overline{\eta}_{22}\overline{\eta}_{33}$. Combining Eqs. (23) and (24) gives an evolution equation for $\boldsymbol{\varepsilon}_v$:

$$\overline{\mathbf{V}}\dot{\boldsymbol{\varepsilon}}_v = \overline{\mathbf{C}}_{ev}(\boldsymbol{\varepsilon} - \boldsymbol{\varepsilon}_p - \boldsymbol{\varepsilon}_v) \tag{25}$$

The total stress may then be expressed in terms of strains as

$$\boldsymbol{\sigma} = \overline{\mathbf{C}}_0(\boldsymbol{\varepsilon} - \boldsymbol{\varepsilon}_p) + \overline{\mathbf{C}}_{ev}(\boldsymbol{\varepsilon} - \boldsymbol{\varepsilon}_p - \boldsymbol{\varepsilon}_v) \tag{26}$$

6.3.3 Temperature-dependent hardening and viscoelastic damage functions

Post-yield properties such as the plastic hardening functions and viscoelastic damage stiffness and damping must be expressed in terms of the reduced equivalent plastic strain. This was done by using equations for the unloading and reloading stress–strain response in terms of the damage moduli, damping and plastic strain. Parameters H_{ij}, $\overline{E}_{ii}$, $\overline{G}_{ij}$, $\overline{E}_{evii}$, $\overline{G}_{evij}$ and $\overline{\eta}_{ij}$ were then extracted by fitting the unloading and reloading equations to experimental uniaxial and shear hysteresis curves. After this, uniaxial and shear plastic strain were converted to reduced equivalent plastic strain $\hat{\varepsilon}_p$.
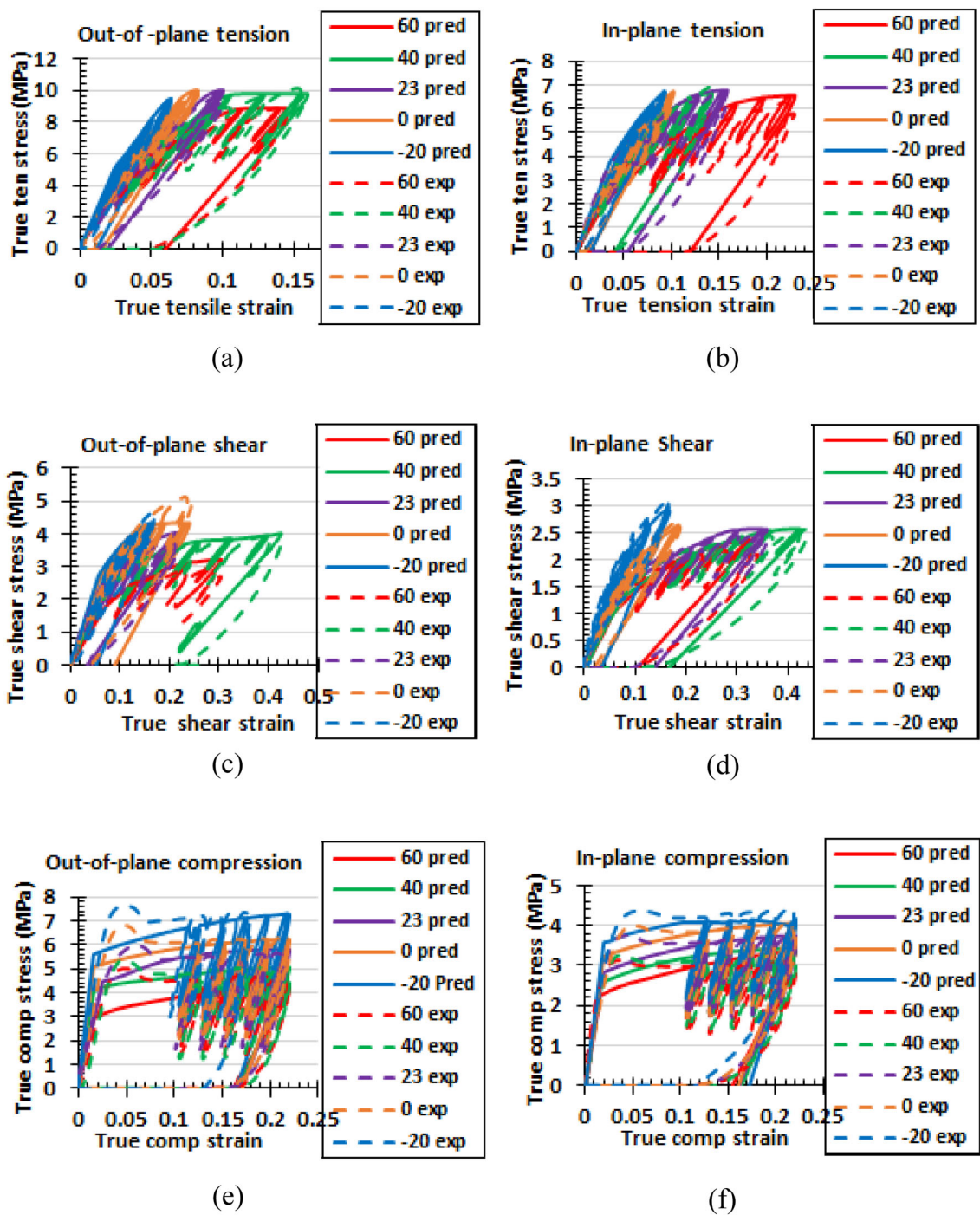
Fig. 16 True stress–strain behavior of Divinycell HCP30 foam at various temperatures: **a** out-of-plane tension, **b** in-plane tension, **c** out-of-plane shear, **d** in-plane shear, **e** out-of-plane compression and **f** in-plane compression

From Eq. (16), we use uniaxial and shear test results to get the equivalent plastic strain:

$$\hat{\varepsilon}_p = \begin{cases} \int_0^{\varepsilon_{pii}} \dfrac{\sigma_{ii}}{f_{33}^c} d\varepsilon_{pii}, & compression/tension \\ \int_0^{\gamma_{pij}} \dfrac{\tau_{ij}}{f_{33}^c} d\gamma_{pij}, & shear \end{cases} \quad (27)$$

where σ_{ii} and τ_{ij} are functions of plastic strain component ε_{pii} and γ_{ij}, respectively. The resulting normalized flow stress or plastic hardening function, damage moduli and viscoelastic damping at various temperatures are plotted in terms of the reduced equivalent plastic strain. Figure 12a–c shows how hardening curves in the out-of-plane direction vary with temperature. Equations used to describe these

curves and results for the in-plane directions are given in Appendix B. Normalized hardening functions increase as the temperature increases.

Temperature variations of viscoelastic damage functions $\overline{E}_0$, $\overline{E}_{ev}$, and $\overline{\eta}$, in the out-of-plane directions are given in Figs. 13, 14 and 15. Appendix B shows temperature variations of in-plane viscoelastic damage functions as well as the functions used to describe these functions. The equilibrium and intermediate moduli $\overline{E}_0$ and $\overline{E}_{ev}$ decreased with increasing strain and increasing temperature. On the other hand, $\overline{\eta}$ increased with increasing strain and decreased with increasing temperature.

6.4 Predicted stress–strain response

The elastic, plastic and viscoelastic properties and functions are incorporated into an ABAQUS Explicit user-defined material (VUMAT) subroutine to simulate uniaxial compression and tension, and simple shear material responses. Development of the VUMAT is discussed in Tong et al. (2020). Figure 16a–f show that predicted and experimental results for Divinycell HCP30 foam compared well in out-of-plane and in-plane direction under uniaxial tension, compression, and shear loadings.

7 Model validation

To validate the material constitutive equation, experiments were conducted on foam sheets 25.4 mm wide by 25.4 mm long and 12.7 mm thick with a 15.24 mm diameter hole in the center (see Appendix A) at various temperatures. The foam sheets were cut from Divinycell HCP30 foam panels so that they could be subjected to tension in the 3-direction (see Fig. 1 for material orientation). The sheets were displacement-controlled tension with a rate of 1.27 mm/s until they broke. The ABAQUS Explicit finite element mesh of the foam sheet is shown in Fig. 17. Here, continuum C3D8R elements were used, and the mesh size was determined by a convergence study. The temperature dependent VUMAT was used to describe foam material response.

The strains in the sheet just before failure are compared between ABAQUS and the DIC strains from the experiment at + 23 oC in Fig. 18. Note that these are elastic–plastic strains for a transversely isotropic foam and although similar, they are not what is expected for linear elastic material. Overall, there is a good comparison between them considering PVC foams are not manufactured as perfect cellular constructs. Cells sizes vary and are randomly distributed. This imperfection is not necessarily considered a manufacturing defect, but the randomness of cell size and wall thickness does present problems in numerical simulations based on homogenized material properties. The FEA predictions will
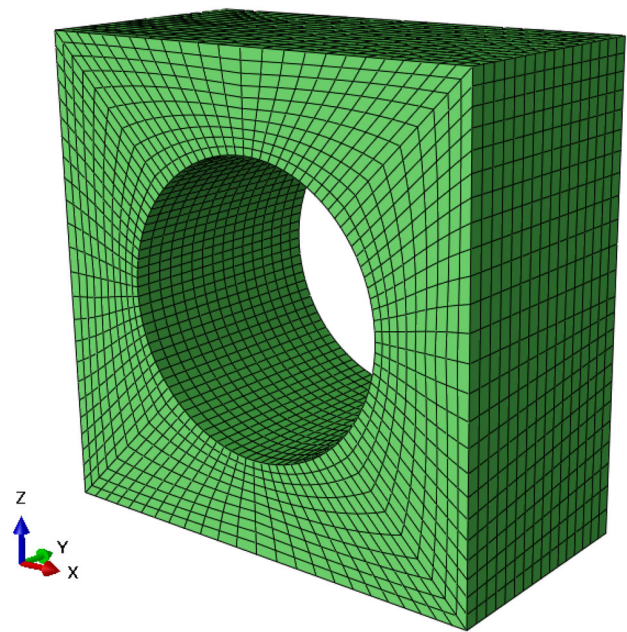

Fig. 17 Finite element mesh of foam with hole loaded in tension

never completely match the strain distributions portrayed in the DIC because there will be small pockets of foam that have higher density or lower density than the average density of Divinycell HCP30 foam. A pocket with higher density will have higher modulus and flow stress than predicted and vice versa. For instance, one may notice small pockets of high tensile DIC yield strains e33 at the top of the sheet and wider compression DIC yield bands in strain e11 at the side of the sheets than what are predicted by the FEA.

In addition to strain distributions, the force–displacement response on the sheet during the experiments at − 20, + 23 and + 60 °C are compared to ABAQUS predictions at these temperatures in Fig. 19. Except for the experiment at + 60 °C, there is also a good comparison between ABAQUS prediction and experimental results. The maximum difference between ABAQUS and experimental prediction at + 60 °C is 17%, and this difference is a consequence of the curve fitting functions that were used to generate temperature-dependent elastic–plastic viscoelastic damage properties.

8 Conclusions

In this research, we characterize and develop predictive equations for elastic and post-yield behavior of Divinycell HCP30 foams over temperatures ranging from − 40 to + 60 °C. The equations will be useful in predicting how sandwich core materials behave over a wide range of environmental temperatures. Experiments were conducted on the foam in
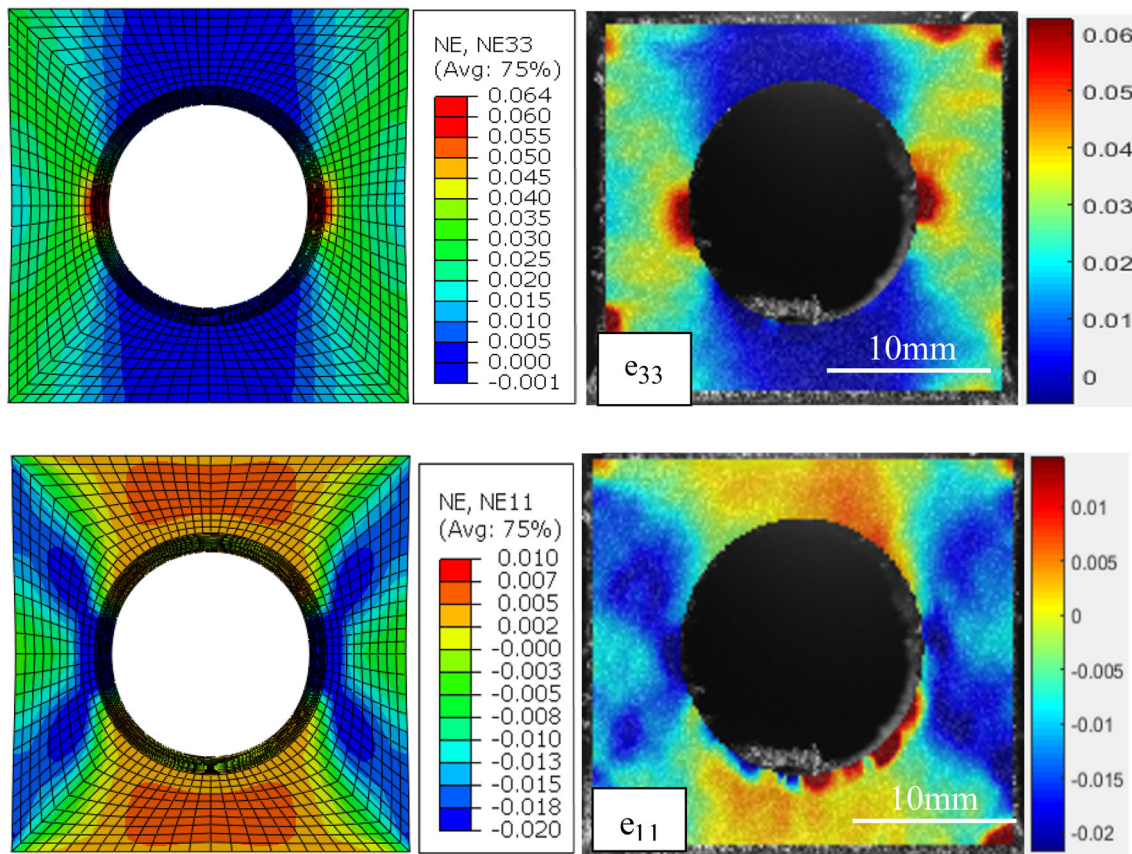
Fig. 18 Comparison of strain distribution in foam sheet at 23 °C between ABAQUS and experiment (DIC results)
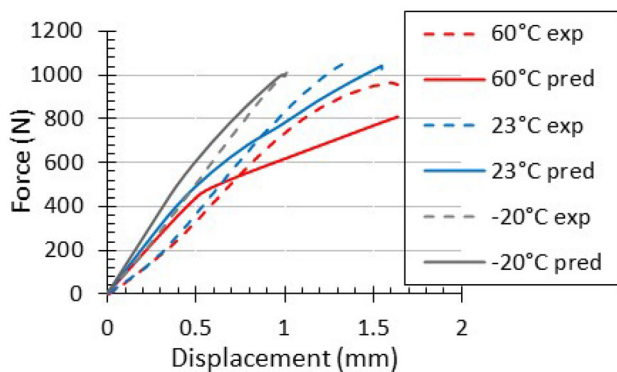

Fig. 19 Force–displacement response of sheet with hole

cyclic tension, compression, and shear and monotonic biaxial tension and compression in the environmental chamber of an MTS servo-hydraulic machine. We found that while elastic modulus and yield strengths decreased linearly with increasing temperature, Poisson's ratio did not vary over this temperature range. Post yield behavior involved plasticity, viscoelasticity, and damage. An elastic–plastic viscoelastic damage model was used to predict post-yield behavior of the foam at different temperatures. The temperature dependent foam material constitutive equations were incorporated into ABAQUS Explicit with a user-defined material subroutine and used to simulate uniaxial and shear foam response. The temperature dependent foam material equations were further validated with experiments on foam sheets with a central hole loaded in tension and at various temperatures. Good comparisons were found between ABAQUS and experimental results.

Author contributions MHF and ARV conducted experiments, and all authors (MHF, AVR and AKP) developed equations to predict foam response at various temperatures. MHF wrote the main manuscript text; ARV prepared Figures 1–19, 20 and 25–28; AKP ran parametric studies in Figures 12–15 and 25–28. All authors reviewed the manuscript.

Data availability The data that supports the findings of this research are available on request from the corresponding author, MHF.

Declarations

Appendix A Specimen geometries

Figures 20, 21 and 22 show the geometry of compression, tension, and shear specimens.
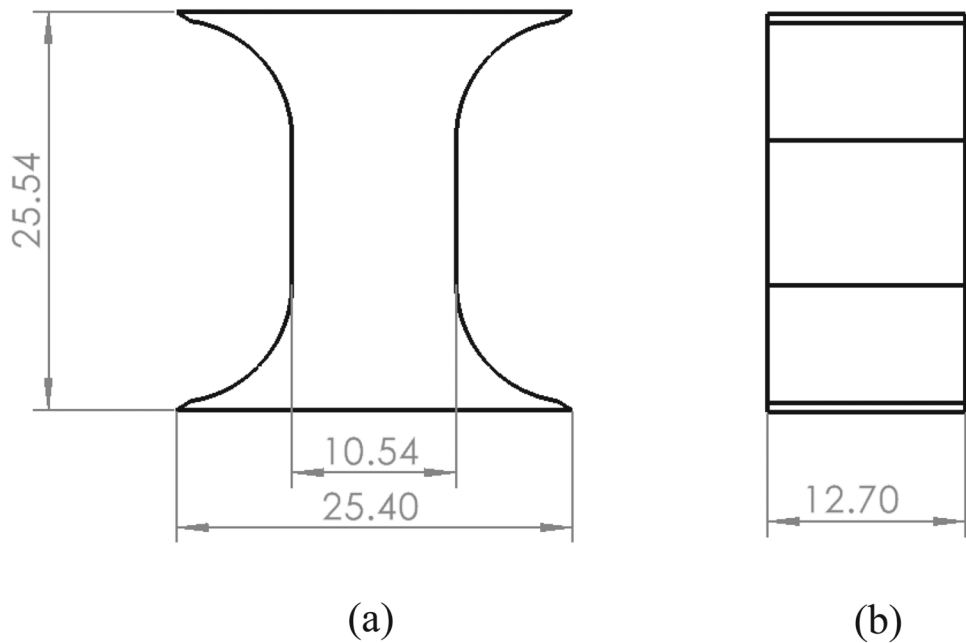
Figure 23a, b show the geometry of Maltese cross specimen used for biaxial tension and compression tests.

The geometry of the foam sheet with hole used to validate model is given in Fig. 24a, b.

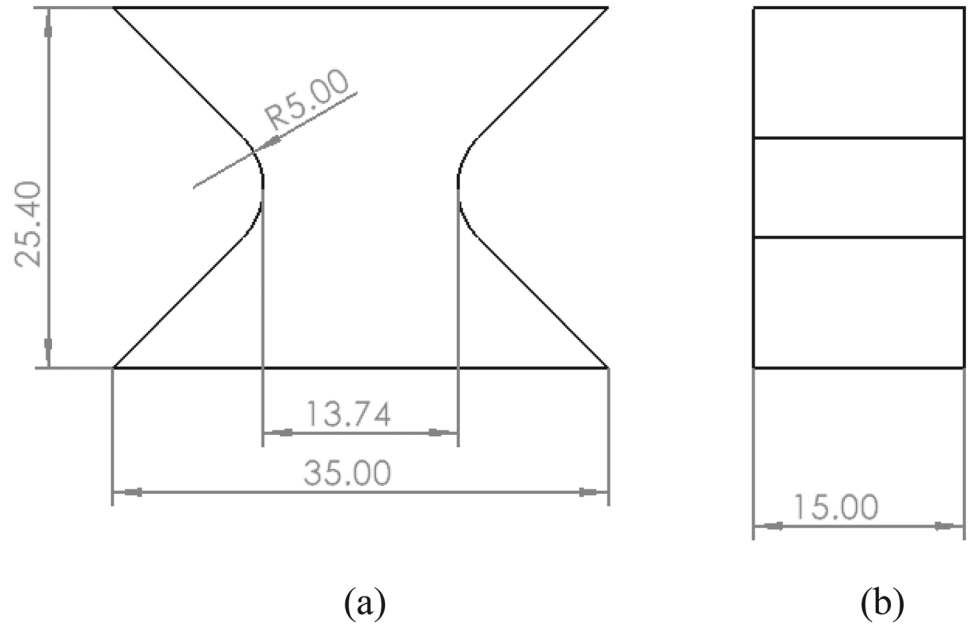**Fig. 20** Geometry of compression specimen: **a** front view and **b** side view (all dimensions in mm)
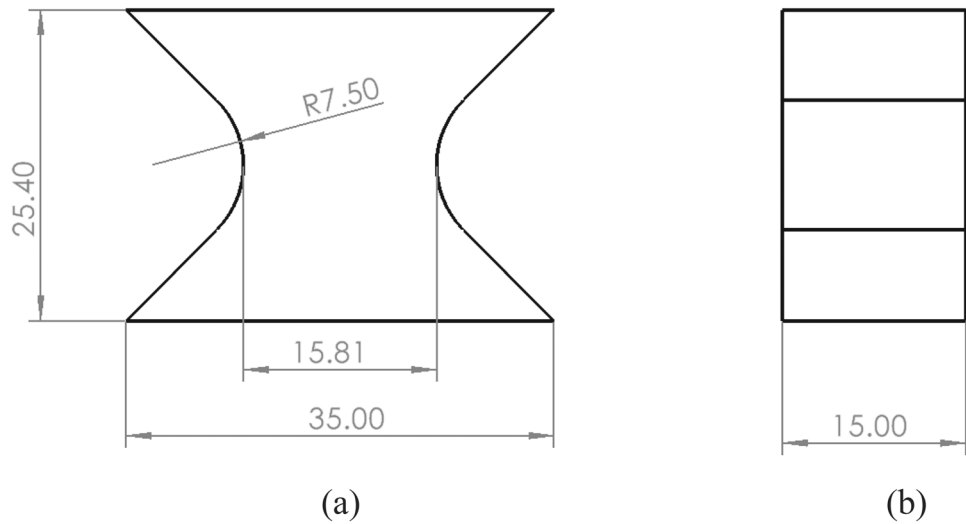
Fig. 21 Geometry of tension specimen: **a** front view and **b** side view (all dimensions in mm)
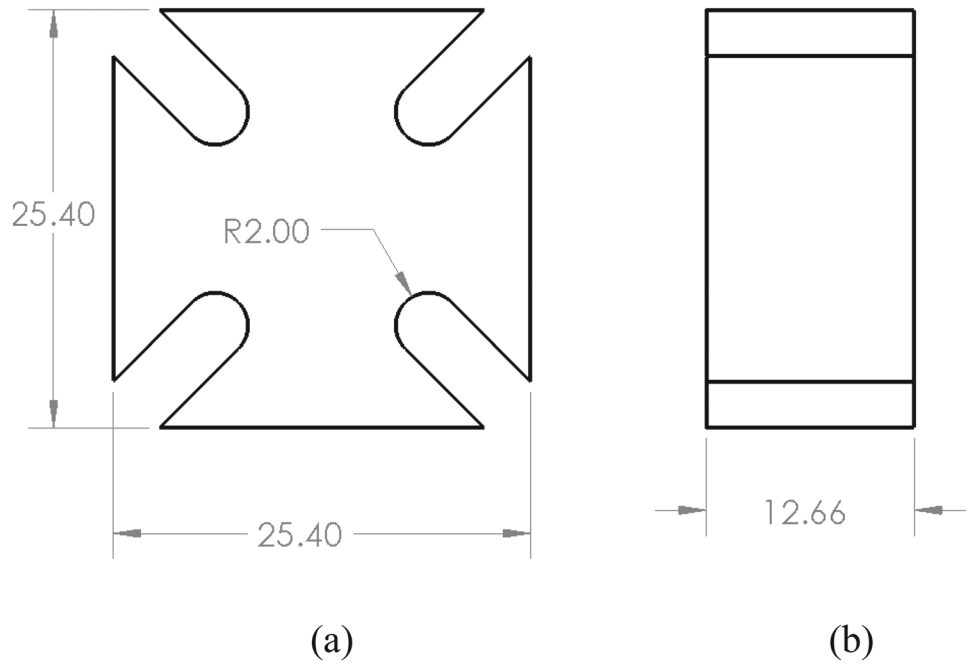
Fig. 22 Geometry of shear specimen: **a** front view and **b** side view (all dimensions in mm)

(a)   (b)

Fig. 23 Geometry of Maltese cross specimen: **a** front view and **b** side view (all dimensions in mm)

(a)   (b)

Appendix B Elastic–plastic viscoelastic damage functions

A general expression for plastic hardening function H_{ij} is

$$H_{ij} = \left(1 + a\left(1 - \exp^{(-b\hat{\varepsilon}_p)}\right)\right) \tag{28}$$

where the coefficients a and b are functions of temperature. Experimental and predicted hardening functions under uniaxial tension, compression, and shear loading, with respect to equivalent plastic strain at temperatures ranging from -40 to $+60$ °C for Divinycell HCP30 foams in-plane directions are shown in Figs. 25.
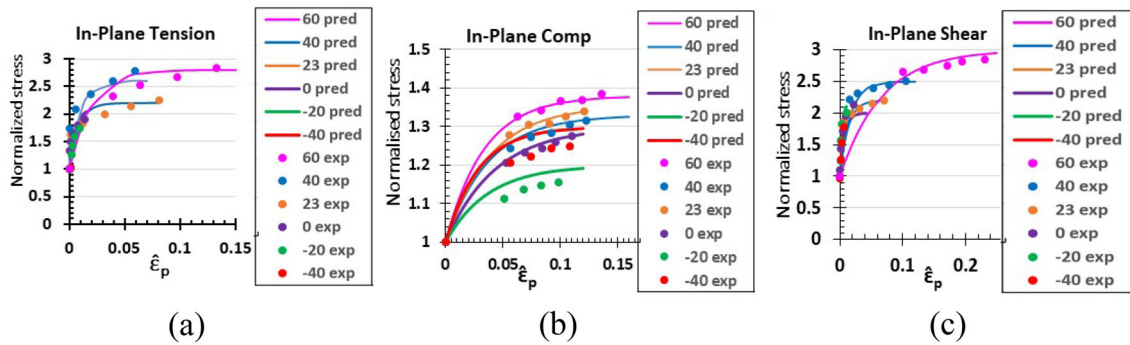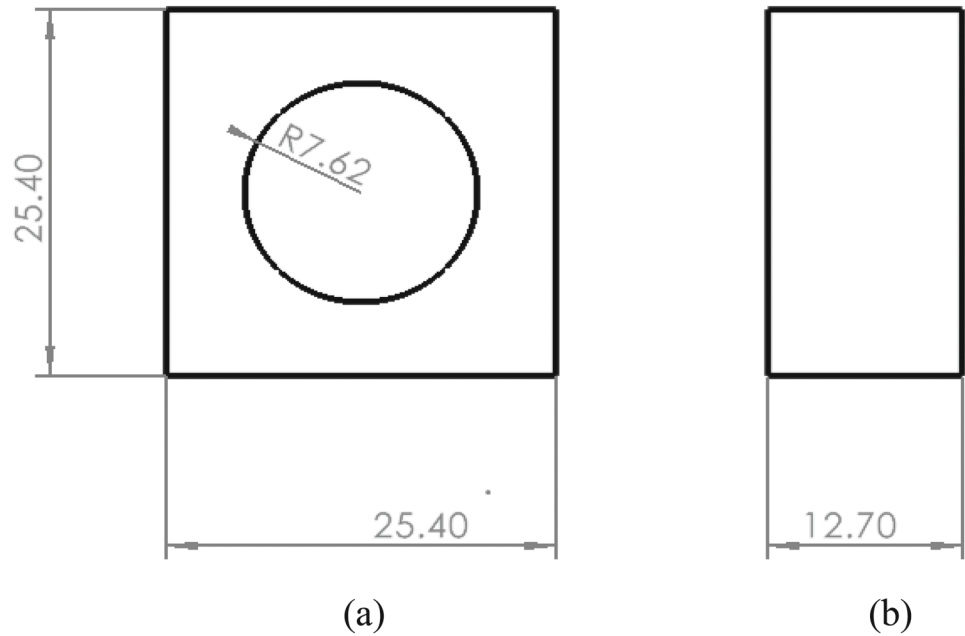
The elastic modulus of the equilibrium spring $\overline{E}_{ij}$ is given by

$$\overline{E}_{ij} = E_{ij}\left(1 - c\left(1 - \exp^{(-d\hat{\varepsilon}_p)}\right)\right) \tag{29}$$

where E_{ij}, c and d are functions of temperature. The elastic modulus of the intermediate spring $\overline{E}_{ev\cdot ij}$ is given by

$$\overline{E}_{ev\cdot ij} = E_{ev\cdot ij}\left(1 - e\left(1 - \exp^{(-f\hat{\varepsilon}_p)}\right)\right) \tag{30}$$

Fig. 24 Geometry of sheet with hole: **a** front view and **b** side view (all dimensions in mm)

(a)　　　　　　　　　(b)

(a)　　　　　　　(b)　　　　　　　(c)

Fig. 25 In-plane hardening: **a** tension, **b** compression and **c** shear

where $E_{ev \cdot ij}$, e and f are functions of temperature. Finally, the viscoelastic damping $\overline{\eta}_{ij}$ is given by

$$\overline{\eta}_{ij} = \eta_{ij}\left(1 + g \log_{10}\left(1 + h\hat{\varepsilon}_p\right)\right) \tag{31}$$

where the initial value of η_{ij} and the coefficients g and h are functions of temperature. Divinycell HCP30 foam viscoelastic damage functions, $\overline{E}_0$, $\overline{E}_{ev}$, and $\overline{\eta}$, in the in-plane at different temperatures are shown in Figs. 26, 27 and 28.

Appendix C Biaxial yield stress calculations

The biaxial loads in the Maltese cross specimen are calculated from MTS machine load and displacement using simple geometric relations given below. The 4-bar link apparatus had two different setups: one with equal length links and the other with two long opposing bars perpendicular to short opposing bars.

Displacements

In the case of tension, the MTS machine actuator arm moves down, and this causes the links to move down and outward in horizontal direction as depicted in Fig. 29. This motion induces tension on the specimen. The solid lines show the initial position, and the dotted line shows the position after displacement. The opposite motion caused compression. In compression mode, the MTS actuator arm moves up, the link moves up and inward pushing on the specimen. The tension or compression displacement Δ is calculated using Pythagoras' theorem and is given by the following equation:

$$\Delta = \begin{cases} H + \sqrt{(L^2 - (V - \delta)^2}, & tension \\ H - \sqrt{(L^2 - (V - \delta)^2}, & compression \end{cases} \tag{32}$$

where δ is the displacement of the MTS machine actuator, H is the horizontal length from centerline of the specimen to

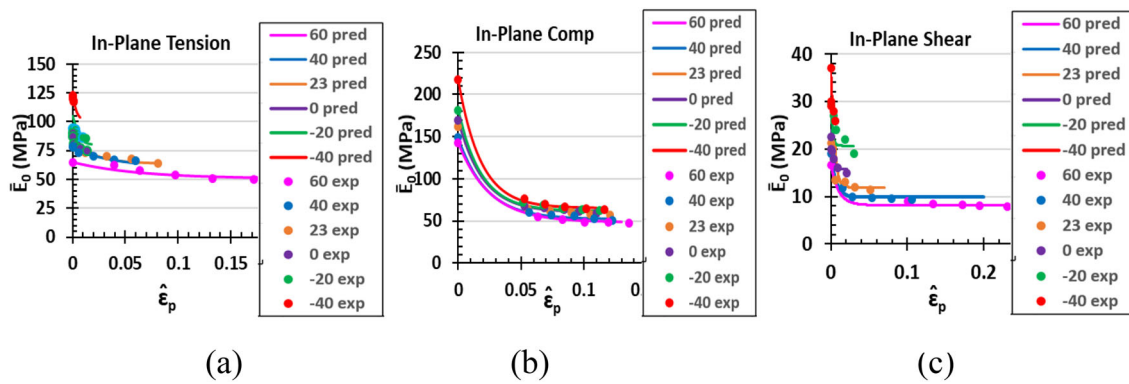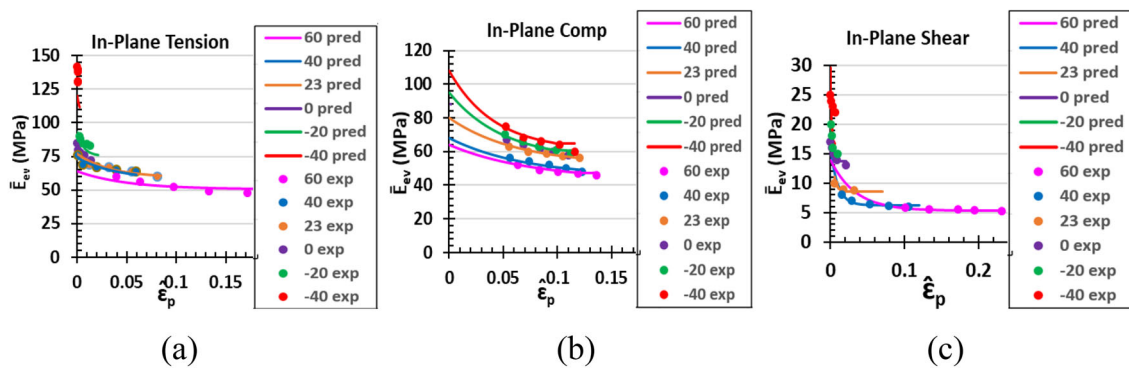**Fig. 26** In-plane $\overline{E}_0$: **a** tension, **b** compression and **c** shear

Fig. 27 In-plane $\overline{E}_{ev}$: **a** compression, **b** tension and **c** shear
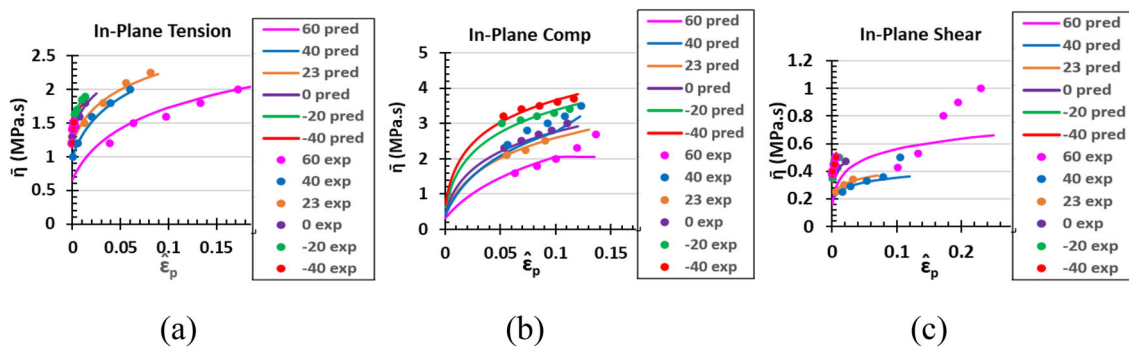

Fig. 28 In-plane $\overline{\eta}$: **a** compression, **b** tension and **c** shear

the end of the link, V is the vertical length from center of the specimen to the end of the link and L is the length of the link.

Forces

The Maltese cross specimens were cut in in-plane (1–2 plane) and out-of-plane (1–3 or 2–3 plane) orientations as shown in Fig. 3. Forces on the specimens depend on the length of link (long or short) as well as whether it was an in-plane and out-of-plane specimen. Force equilibrium at the pin nodes connecting links to the specimen was used to derive the formulas below.
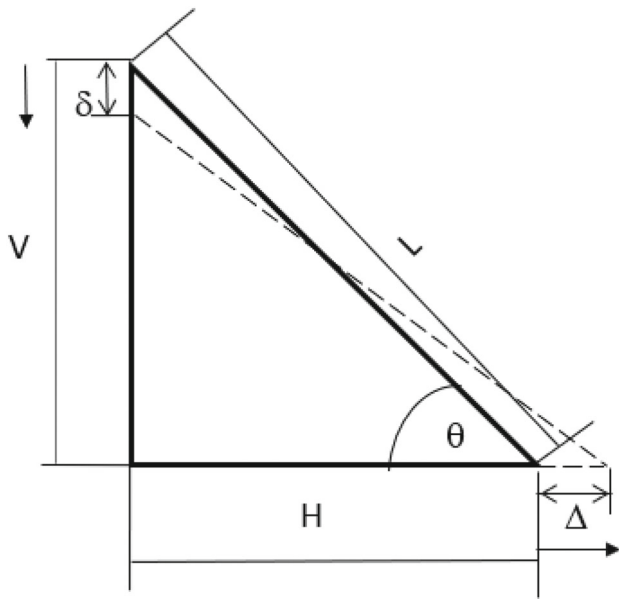
In plane specimen

The force on in-plane specimen is given by

$$F_l = \frac{F\Delta_l}{2\Delta_l \tan\theta_l + 2\Delta_s \tan\theta_s} \tag{33}$$

$$F_s = \frac{F\Delta_s}{2\Delta_l \tan\theta_l + 2\Delta_s \tan\theta_s} \tag{34}$$

where F is total force imparted by the MTS machine; F_l and F_s are the forces in the specimen associated with long and short bars, respectively; Δ_l and Δ_s are the displacement

Fig. 29 Biaxial motion in tensile mode

$$F_l = \frac{kF\Delta_l}{2k\Delta_l \tan\theta_l + 2\Delta_s \tan\theta_s} \tag{35}$$

$$F_s = \frac{F\Delta_s}{2k\Delta_l \tan\theta_l + 2\Delta_s \tan\theta_s} \tag{36}$$

where k is the ratio between uniaxial yield strength in 3-direction to the 1- or 2-direction.

When short links are in the 3-direction and the long links are in the 1-direction, the force in specimen is given by

$$F_s = \frac{kF\Delta_s}{2\Delta_l \tan\theta_l + 2k\Delta_s \tan\theta_s} \tag{37}$$

$$F_l = \frac{F\Delta_l}{2\Delta_l \tan\theta_l + 2k\Delta_s \tan\theta_s} \tag{38}$$

induced by long bars and short bars respectively; and θ_l and θ_s are the angles subtended by the long and short bars, respectively, as shown in Figs. 29. If all four bars are of equal length, then $F_l = F_s$, $\Delta_l = \Delta_s$ and $\theta_l = \theta_s$.

Out-of-plane specimen

The force in the out-of-plane specimen depends on whether the long links are in the 3-direction or not. When the long links are in the 3-direction and short links are in the 1- or 2-directions, the specimen force is given by

Yield stresses

Typical force–displacement curves from the out-of-plane biaxial tension test is shown in Fig. 30a, b. The yield strength is defined by loss of linearity in force–displacement response. The yield point is determined on the force–displacement curve by extrapolating a straight line in the initial linear region. The point where the curve deviates from the straight line is the yield point as indicated by the dots in Fig. 30a, b. Yield strengths at this point are calculated by dividing these forces by the cross-sectional area of the gage section in the Maltese cross section, which is equal to 129 mm^2.

Fig. 30 Yield points defined from **a** In-plane force–displacement and **b** out-of-plane force–displacement
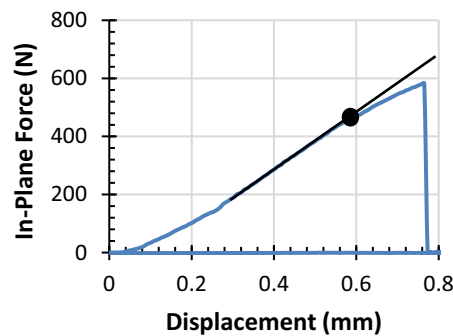
(a)
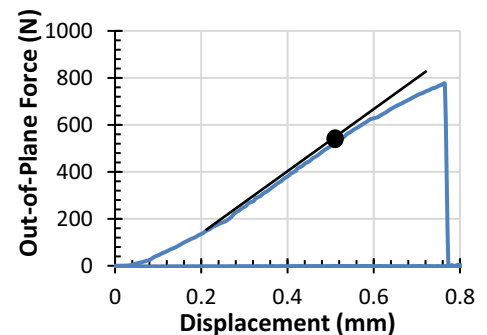
(b)

References

Barroso A, Correa E, Freire J, París F (2018) A device for biaxial testing in uniaxial machines. Design, manufacturing and experimental results using cruciform specimens of composite materials. Exp Mech 58:49–53

DIAB (2023) Technical data Divinycell H. DIAB web site. https://diab-media.azureedge.net/eyajkrhd/datasheet-diab-divinycell-h-march-23-rev-temp-dnv-si.pdf. Accessed 25 Sept 2023

Hoo Fatt MS, Vedire AR (2022) Mechanical properties of marine polymer foams in the arctic environment. Mar Struct 86:103308

Hoo Fatt MS, Zhong C, Gadepalli PC, Tong X (2021) Crushable multiaxial behavior of sandwich foam cores: pressure vessel experiments. J Sandw Struct Mater 23(6):2028–2063. https://doi.org/10.1177/1099636220909797

Hoo Fatt MS, Vedire AR, Pakala AK (2023) Crushable polymer foam behavior at cold temperatures. J Sandw Struct Mater. https://doi.org/10.1177/10996362231158612

Kim DH, Kim JH, Kim HT, Kim JD, Uluduz C, Kim M, Kim SK, Lee JM (2023) Evaluation of PVC-type insulation foam material for cryogenic applications. Polymers (Basel) 15(6):1401

Li S, Sitnikova E, Liang Y, Kaddour A-S (2017) The Tsai–Wu failure criterion rationalised in the context of UD composites. Compos A Appl Sci Manuf 102:207–217

Lindholm C-J, Jones J, Olsson D (2016) Dynamic and quasi static testing of interpenetrating polymer network (IPN) foam cores. In: Presented at international symposium on dynamic response and failure of composite materials (DRaF 2016), Ischia, Italy, September 6–9, 2016

Medellín LFP, Diosdado De la Peña JA (2017) Design of a biaxial test module for uniaxial testing machine. Mater Today Proc 4(8):7911–7920

Taher T, Thomsen OT, Dulieu-Barton JM, Zhang S (2012) Determination of mechanical properties of PVC foam using a modified Arcan fixture. Compos Part A 43:1698–1708

Thomas T, Mahfuz H, Carlsson LA, Kanny K, Jeelani S (2002) Dynamic compression of cellular cores: temperature and strain rate effects. Compos Struct 58(4):505–512

Tong X, Hoo Fatt MS, Zhong C, Alkhtany M (2020) Predicting anisotropic crushable polymer foam behavior in sandwich structures. Multiscale Multidiscip Model Exp Des 3:245–264. https://doi.org/10.1007/s41939-020-00071-5

Tong X, Hoo Fatt MS, Vedire AR (2021) A new crushable foam model for polymer-foam core sandwich structures. Int J Crashworth 27(5):1460–1480. https://doi.org/10.1080/13588265.2021.1959170

Tsai SW (1984) A survey of macroscopic failure criteria for composite materials. J Reinf Plast Compos 3(1):40–62

Wierzbicki T, Doyoyo M (2002) Determination of the local stress-strain response of foams. J Appl Mech 70(2):204–211

Williams DA, Lopez-Anido RA (2014) Strain rate and temperature effects of polymer foam core material. J Sandw Struct Mater 16(1):66–87

Zhang S, Dulieu-Barton JM, Fruehmann RK, Thomsen OT (2012) A methodology for obtaining material properties of polymeric foam at elevated temperatures. Exp Mech 2:3–15